RSC Advances

PAPER

View Article Online
View Journal | View Issue

Cite this: *RSC Adv.*, 2019, **9**, 22559

Oxygen vacancy regulation in Nb-doped Bi_2WO_6 for enhanced visible light photocatalytic activity

Hao Chen,[a] Changteng Zhang,[a] Ya Pang,[a] Qianhong Shen,*[ab] Yang Yu,[a] Yuxuan Su,[a] Jiabang Wang,[a] Fang Zhang[b] and Hui Yang*[ab]

Received 16th April 2019
Accepted 15th July 2019

DOI: 10.1039/c9ra02862e

rsc.li/rsc-advances

Novel Nb-doped Bi_2WO_6 nanosheets have been successfully synthesized by a simple hydrothermal method. XRD, Raman spectra, XPS and SEM were adopted to analyze the structure and morphology of the samples, then the structure-dependent optical properties, photoelectric behavior and photocatalytic activities were investigated, and the structure–property relationship was also discussed. The results show that doping Nb^{5+} can increase the oxygen vacancies in the Bi_2WO_6 lattice and reduce the optical band gap of Bi_2WO_6. The oxygen vacancies also act as electron traps, which promote the separation of photogenerated carriers. Hence, compared with the pure Bi_2WO_6, the as-prepared Nb-doped Bi_2WO_6 nanosheets exhibit enhanced visible-light photocatalytic activity for removing contaminants in water such as rhodamine B and tetracycline.

1. Introductions

Heterogeneous photocatalysis offers tremendous potential for use in the field of environmental remediation and the conversion of photons into chemical energy.[1–3] In recent decades, TiO_2 semiconductors have become a typical photocatalyst for decomposition of organic contaminants and water splitting due to their good physical and chemical properties.[4,5] However, as a UV-driven photocatalyst, TiO_2 can only respond to UV light, which is less than 4% of sunlight reaching the Earth's surface.[6,7] In order to make better use of solar energy, more and more researchers have turned their attention to visible-light-driven photocatalysts.

As a simple Aurivillius-type compound, bismuth tungstate featuring its layered configuration consisting of alternating $(Bi_2O_2)^{2+}$ layers and $(WO_4)^{2-}$ octahedral layers displayed excellent visible light photocatalytic activity.[8–10] However, for intrinsic semiconductors, the fast recombination of photo-generated electrons and holes seriously limited their quantum efficiency, which was also a key issue of pure Bi_2WO_6 that needs to be solved. Many strategies have been proposed to promote the separation of photo-generated carries, such as loading noble metals, constructing heterojunctions, doping ion elements and so on.[11–14] In these strategies, ion doping can introduce the doping level into the band gap, therefore not only reducing the recombination of photo-generated electron–hole pairs, but also further expanding light absorption to the visible wavelength range. It has been reported that F, Br, and N can partially substitute the O-site, therefore raising the valence band,[15–17] whereas metallic ions such as Cd, Y, Gd can partially substitute the Bi-site.[18–20] Furthermore, co-doping such as F–Ce and lanthanide elements can efficiently expand the absorption range to visible light.[21–23] W-site substitution in Bi_2WO_6 systems was another effective modification route, the different d orbital structure of heterogeneous ions substituting W^{6+} would causes a change in the crystal structure and symmetry. Moreover, the electron mobility can be promoted due to the difference in the orbital energies of the heterogeneous ions, thereby improving photoelectron–hole separation efficiency.[24]

In this paper, Nb^{5+} was applied to partially substitute W^{6+} to modify the crystal structure of Bi_2WO_6, as well as to construct oxygen vacancies serving as an electron trap and widening the valence band, which would promote the separation of photo-generated carriers and improve the absorption efficiency of sunlight.[25,26] To the best of our knowledge, this is the first time Nb-doped Bi_2WO_6 photocatalysts have been reported. The mechanism of the effects of Nb substitution on the Bi_2WO_6 photocatalysts was studied on the basis of the crystal structure, electronic structure, and morphology of Bi_2WO_6 photocatalysts.

2. Experimental

2.1 Materials

Chemicals (AR grade) involved in this work including bismuth nitrate ($BiN_3O_9 \cdot 5H_2O$), tungstic acid (H_2WO_4), oxalic acid ($H_2C_2O_4 \cdot 2H_2O$), ammonia ($NH_3 \cdot H_2O$), niobium oxide (Nb_2O_5), rhodamine B (RhB) and tetracycline (TC) were obtained commercially from Aladdin Reagent Co. Ltd. All chemicals were analytical grade reagents and were used without further purification.

---

[a] *State Key Laboratory of Silicon Materials, School of Materials Science and Engineering, Zhejiang University, Hangzhou, P. R. China 310027. E-mail: 21826027@zju.edu.cn; s_qianhong@163.com*

[b] *Zhejiang-California International NanoSystems Institute, Zhejiang University, Hangzhou, P. R. China 310058*

2.2 Preparation

The Nb-doped Bi_2WO_6 nanosheets were synthesized *via* a simple one-step hydrothermal method. Firstly, 2 mmol of $Bi(NO_3)_3 \cdot 5H_2O$ was dissolved in 40 mL of oxalic acid solution with concentration of 1.25 mol L^{-1}, and 1 mmol of H_2WO_4 was added dropwisely to $Bi(NO_3)_3$ solution. And then, a desired amount of Nb_2O_5 was then added into the above solution. Then, the pH value of the mixture was adjusted to 7 with 1 mol L^{-1} of $NH_3 \cdot H_2O$. Finally, the mixture was added into a 100 mL of Teflon-lined autoclave and filled with deionized water to 80% of the total volume. Then the autoclave was heated in an oven at 180 °C for 24 h. After cooling the autoclave to room temperature naturally, the obtained yellow precipitate was washed with deionized water and absolute ethanol and then dried at 60 °C in an oven. The resultant samples with expected molar ratio of $Nb : W = 0.02$, 0.05, and 0.07 were denoted as BWO-Nb2, BWO-Nb5 and BWO-Nb7, respectively. For comparison, the pure Bi_2WO_6 was prepared through the similar method and denoted as BWO.

2.3 Characterization

Crystal structure of the as-prepared samples were characterized by powder X-ray diffraction on a PANalytical diffractometer (APEXII, Bruker, Germany) with Cu Kα radiation ($k = 0.1542$). UV-vis diffuse reflectance spectra were recorded on a UV-vis spectrophotometer (UV-4100, Hitachi, Japan) in the range 200–700 nm using $BaSO_4$ as the reference sample. The morphology and particle sizes of simples were determined by scanning electron microscope (SU-8010, Hitachi, Japan). Raman spectra measurement was carried out by a Raman spectrometer (DXR SmartRaman, Thermo Fisher Scientific, USA). X-ray photoelectron spectrometer (VGMK II, Thermo Fisher Scientific, USA) was employed to perform the X-ray photoelectron spectroscopy test. The photoluminescence emission spectra of as-prepared samples were detected on a steady-state spectrometer (FLS920, Edinburgh, UK), and the PL emission spectra were obtained at an excitation wavelength of 325 nm with a Xe lamp. Photoelectrochemical tests were carried out in a three-electrode system with Pt foil as the counter electrode and Ag/AgCl electrode as the reference electrode. The working electrodes were pure Bi_2WO_6 or Nb–Bi_2WO_6 film coated on indium-tin oxide glass (ITO) and with 0.5 mol L^{-1} of Na_2SO_4 solution as electrolyte solution were measured at 0.1 V under visible light ($\lambda > 420$ nm). The electrochemical system (CHI 660E, Chenhua, China) was employed to record the photoelectrochemical experiment results. The electrochemical impedance spectra (EIS) were all measured at 0 V.

2.4 Evaluation of photocatalytic activity

Photocatalytic activities of pure Bi_2WO_6 and Nb-doped Bi_2WO_6 were investigated by degradation of RhB and TC under visible light irradiation ($\lambda > 420$ nm, 300 W Xe lamp), the average light intensity was 23 mW cm^{-2}. First, the 50 mg of photocatalysts were ultrasound-dispersed in an aqueous solution of RhB (100 mL, 10 mg L^{-1}) or 30 mg of photocatalysts were ultrasound-dispersed in an aqueous solution of TC (100 mL, 20 mg L^{-1}). Then, the mixture was magnetically stirred in dark for 30 min to reach an adsorption–desorption equilibrium. Afterward, the photocatalysis reaction was started. During the photocatalysis reaction, 4 mL of mixture was taken at 20 min intervals and was centrifuged to remove the photocatalysts. The concentration of RhB and TC in supernatant fluid was determined by measuring the absorbance at 553 nm and 356 nm respectively by using UV-vis spectrophotometer (U-3010, Hitachi, Japan).

The experimental conditions of the free radical trapping experiment and cycling runs experiment are consistent with the conditions of the photocatalytic degradation experiment, except that an appropriate amount of a radical scavenger is added thereto. The recycled samples are recovered by centrifugation and dried as samples for the next cycle.

3. Results and discussions

3.1 Structure and morphology analysis

XRD patterns of as-prepared samples are shown in Fig. 1a. It can be observed that Bi_2WO_6 with single Aurivillius phase can be synthesized *via* a hydrothermal method. The diffraction peaks of Bi_2WO_6 can be exactly indexed to JCPDS 79-2381. Moreover, the diffraction intensity ratio of $I(113)/I(200)$ of Bi_2WO_6 is less than 2, indicating that the as-prepared samples occur a special anisotropic growth.[27] It can be observed that the (113) and (200) diffraction peaks of Nb-doped Bi_2WO_6 regularly shift to a lower

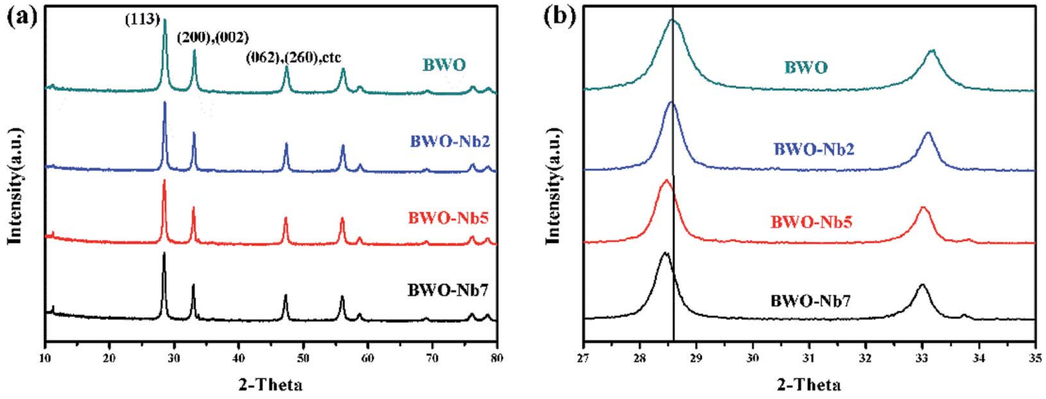

Fig. 1 (a) XRD patterns of BWO, BWO-Nb2, BWO-Nb5, BWO-Nb7, (b) the enlarged XRD patterns located from 27° to 35°.

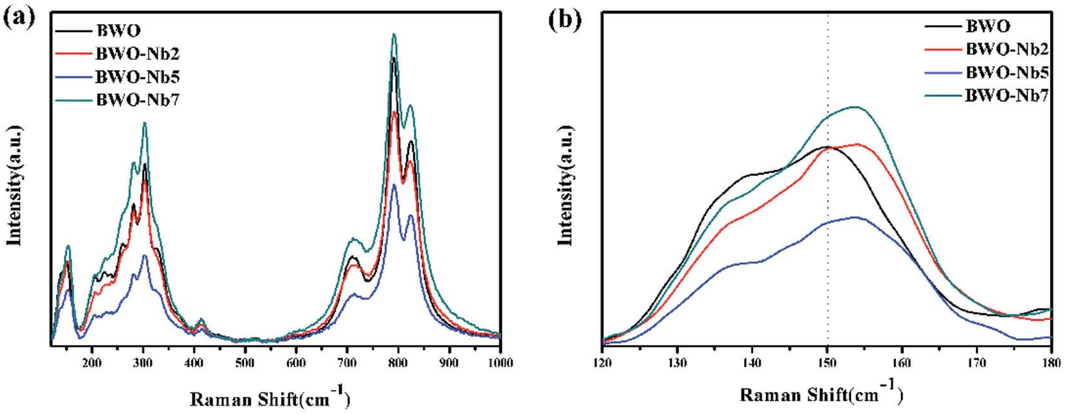

Fig. 2 (a) Raman spectra of BWO, BWO-Nb2, BWO-Nb5, BWO-Nb7; (b) magnified peaks located from 120 cm^{-1} to 180 cm^{-1}.

diffraction angle with the increase of doping amount of Nb element (Fig. 1b). This is mainly because that the replacement of W^{6+} by Nb^{5+} generates oxygen vacancies in Bi_2WO_6, leading to the enlargement of crystal face distance and slight change in crystal structure.[28,29]

Raman spectra of Nb-doped Bi_2WO_6 and pure Bi_2WO_6 are shown in Fig. 2a. The peaks located at 790 and 817 cm^{-1} are related to the symmetric and asymmetric Ag modes of terminal O–W–O, and the band located at 707 cm^{-1} is related to the antisymmetric bridging mode of the tungstate chain.[30] Meanwhile, the bands located at 256, 274 and 296 cm^{-1} are assigned to the bending of apical O–W–O, and the band located at 406 cm^{-1} corresponds to the bending of equatorial O–W–O. The peaks below 170 cm^{-1} can be assigned to translations of the W and B ions. Compared with pure Bi_2WO_6, the peaks of Nb-doped Bi_2WO_6 located in the range of 400–1000 cm^{-1} cannot be observed obvious shift with the increase of Nb doping content, suggesting the vibrational energy of the W–O stretching band and apical O–W–O band are not changed. Whereas, the peaks of Nb-doped Bi_2WO_6 located at 150 cm^{-1} regularly shift to high frequency with increasing Nb doping content. It indicates that the small amount of Nb doping changes the chemical environment of the element, resulting in the change of ion migration energy.[31]

Fig. 3 shows the high-resolution XPS spectra of BWO and BWO-Nb5 samples, respectively. It can be clearly seen from Fig. 3a that the orbital binding energy if Bi, Nb, W and O in the XPS spectrum of BWO-Nb5. In Fig. 3b, the 4d orbital binding

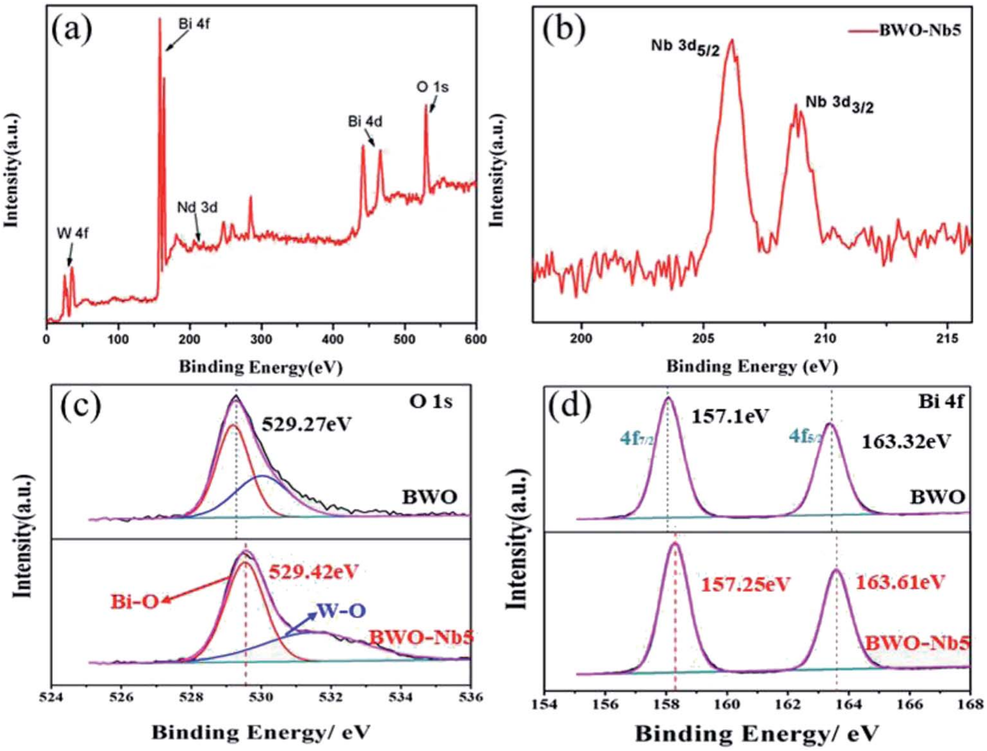

Fig. 3 (a) High-resolution XPS spectra of for BWO-Nb5; (b) Nb 3d spectrum for BWO-Nb5; (c) O 1s spectrum for BWO and BWO-Nb5 samples; (d) Bi 4f spectrum for BWO and BWO-Nb5 samples.

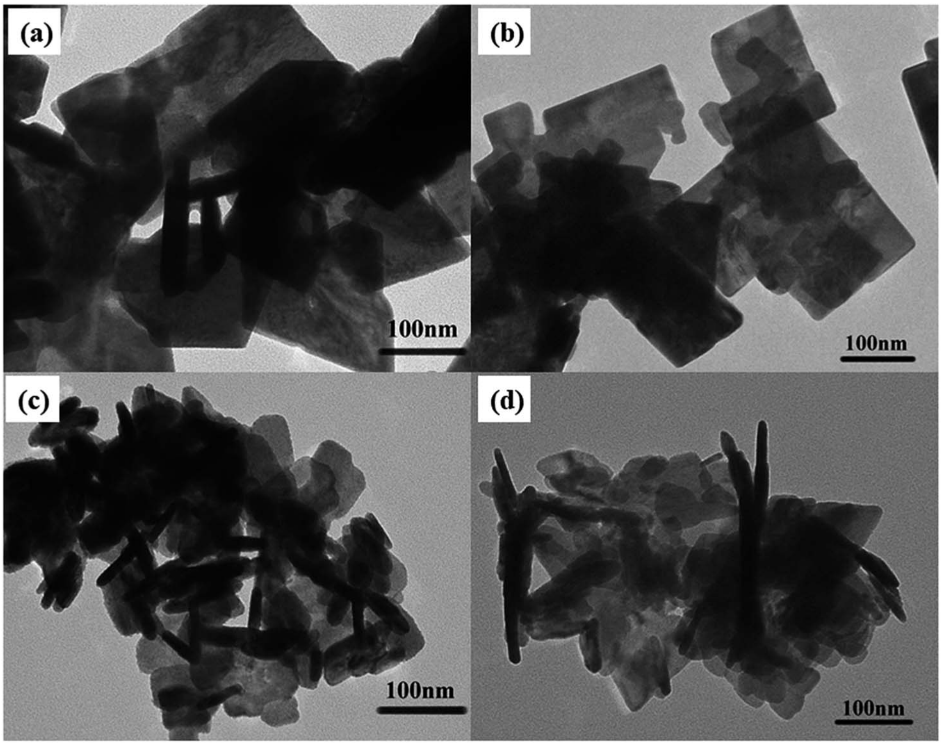

Fig. 4 (a) TEM images of BWO; (b) TEM images of BWO-Nb2; (c) TEM images of BWO-Nb5; (d) TEM images of BWO-Nb7.

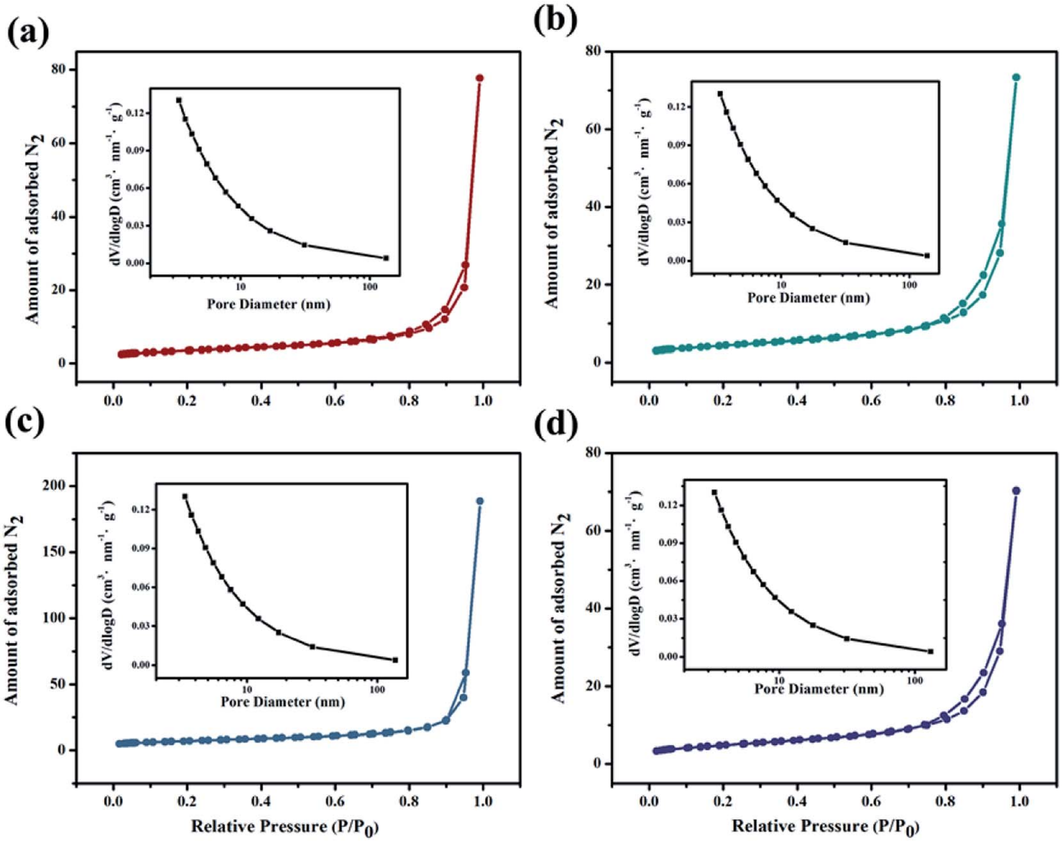

Fig. 5 Nitrogen adsorption–desorption isotherms and pore size distribution curves for prepared samples (a) BWO; (b) BWO-Nb2; (c) BWO-Nb5; (d) BWO-Nb7.

energy of Nb in the BWO-Nb5 sample is 206.2 eV and 208.9 eV corresponds to the Bi–Nb bond and Nb–O band, respectively. In Fig. 3c and d, the XPS spectra correspond to the O 1s and Bi 4f orbital binding energy in the BWO and BWO-Nb5 samples, respectively. Moreover, the binding energy of O 1s and Bi 4f XPS spectra of BWO-Nb5 shift to higher binding energy from 529.27 eV, 157.1 eV to 529.42 eV and 157.25 eV, which is mainly attributed to the high electronic effect of neighboring oxygen vacancies.[9,32] Introducing Nb into the lattice matrix of Bi_2WO_6 formed oxygen vacancy as Nb^{5+} replaces W^{6+}, and the oxygen vacancy can decrease the electron density in the crystal, thereby strengthening the binding energy.[33]

Fig. 4a–d shows the TEM of the prepared BWO and BWO-Nb nanosheets. It can be clearly observed from the figure that the size of the Nb-doped Bi_2WO_6 samples are significantly smaller than that of the pure Bi_2WO_6. At the same time, the thickness of the nanosheets is also greatly reduced. The reduction in size and thickness of the Bi_2WO_6 nanosheets means greater surface area and surface active sites, resulting in greater photocatalytic activity.

The Fig. 5 shows the nitrogen adsorption–desorption isotherm for BWO and BWO-Nb samples. A pore-size-distribution curve was calculated from the desorption branch of nitrogen isotherm by the BJH method. The pore size distribution of the experimentally prepared BWO and BWO-Nb is within 10 nm, which indicates that the doping of Nb atoms does not affect the pore size of Bi_2WO_6. From the adsorption–desorption curve, the surfaces of BWO, BWO-Nb2, BWO-Nb5, and BWO-Nb7 were 12.513 $m^3\ g^{-1}$, 15.617 $m^3\ g^{-1}$, 24.716 $m^3\ g^{-1}$, and 17.129 $m^3\ g^{-1}$, respectively. The BET experimental results further demonstrate that the doping of Nb atoms reduces the particle size of Bi_2WO_6 and thus has a larger surface area.

3.2 Photocatalysis mechanism

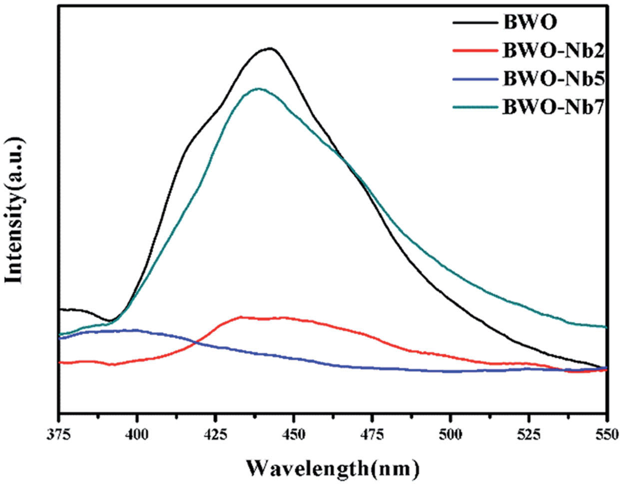

Fig. 7 PL spectra curves of BWO, BWO-Nb2, BWO-Nb5 and BWO-Nb7 samples.

DRS spectra of BWO-Nb5 and BWO samples are exhibited in Fig. 6. It can be seen that the absorption edge of BWO-Nb5 and BWO are observed to be 458 nm and 453 nm, respectively. Nb doping leads to the red shift of absorption edge of Bi_2WO_6. The band gap values of BWO-Nb5 and BWO estimated from the $(\alpha h\nu)^{1/2}$ *versus* photon energy plots are about 2.68 eV and 2.73 eV, respectively.[34] The reduction of optical band gap for Bi_2WO_6 may be resulted from the two factors: (1) the 4d orbital of Nb^{5+} and the 5d orbital of W^{6+} form a new conduction band. (2) The surface oxygen vacancies increase the valence bandwidth of Bi_2WO_6, which makes the valence band of Bi_2WO_6 move up, which enhances the utilization of sunlight.

In order to investigate the separation efficiency of photogenerated carriers in photocatalysis reaction, PL emission spectrum testing was carried out. It can be seen from the Fig. 7 that the emission peaks of the four prepared samples near 430 nm, furthermore, the PL peak intensity of the Nb-doped Bi_2WO_6 sample is lower than that of the pure Bi_2WO_6. The high electron effect of the oxygen vacancies can attract photogenerated electrons, thereby promoting the separation of photogenerated carriers. However, the excessive concentration of oxygen vacancies will become the recombination center of

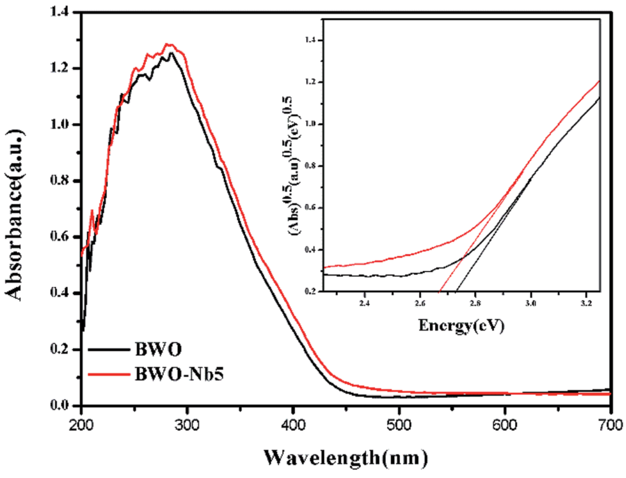

Fig. 6 UV-vis DRS spectra and plots of $(\alpha h\nu)^{1/2}$ *versus* $h\nu$ (the inset) of BWO and BWO-Nb5 samples.

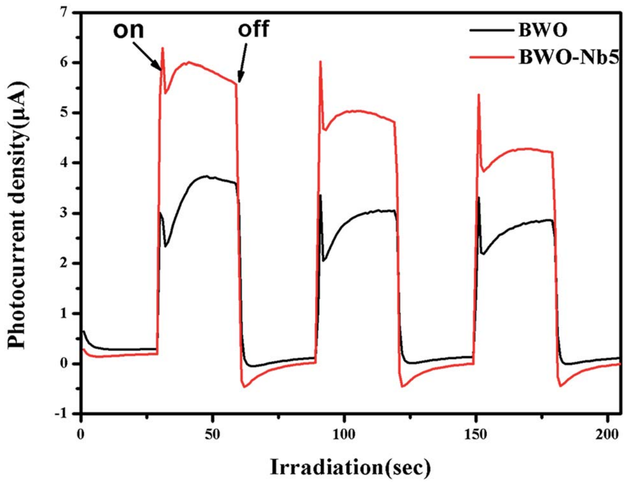

Fig. 8 Photocurrent response of BWO and BWO-Nb5 samples.

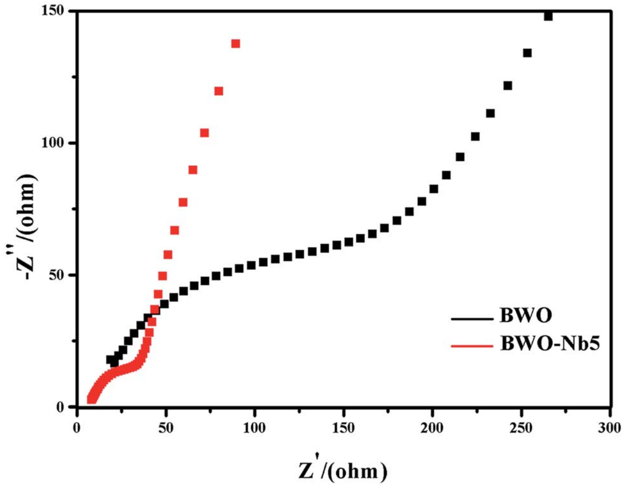

Fig. 9 EIS spectra of BWO and BWO-Nb5 samples.

photo-generated carriers.[35] Therefore, it is observed that with further increasing the Nb doping amount, the PL intensity of BWO-Nb7 increases instead.

The Fig. 8 shows a comparison of the visible-light photocurrent responses contributed by BWO and BWO-Nb5. Both BWO and BWO-Nb5 samples exhibited rapid visible light response photocurrent, whereas BWO-Nb5 samples showed higher photocurrent than BWO samples, indicating more efficient photoinduced charge separation and transfer in BWO-Nb5 samples. It can be seen that the photocurrent from BWO-Nb5 is about 1.85 times higher than the photocurrent from BWO, which indicates that the surface oxygen vacancies generated by the Nb doping greatly promote photogenerated charge transfer.

The electrochemical impedance spectroscopy (EIS) was also adopted to investigate BWO and BWO-Nb5 electrodes, which is another valid electrochemical strategy to measure the transfer and separation efficiency of photo-generated carries. Generally, a smaller EIS arc radius suggests an effective separation of photo-generated carriers and fast interfacial charge transfer. As shown in Fig. 9, the EIS arc radius of BWO-Nb5 is smaller than that of BWO, indicating the higher mobility and separation efficiency of interfacial photo-generated carriers in BWO-Nb5.

3.3 Evaluation of photocatalytic activity

As shown in Fig. 10, Nb-doped Bi_2WO_6 samples exhibit much better photocatalytic activity than pure Bi_2WO_6. The BWO-Nb5 displays the highest photocatalytic efficiency. The first-order linear relationship is revealed by the plots of $\ln(C/C_0)$ *vs.*

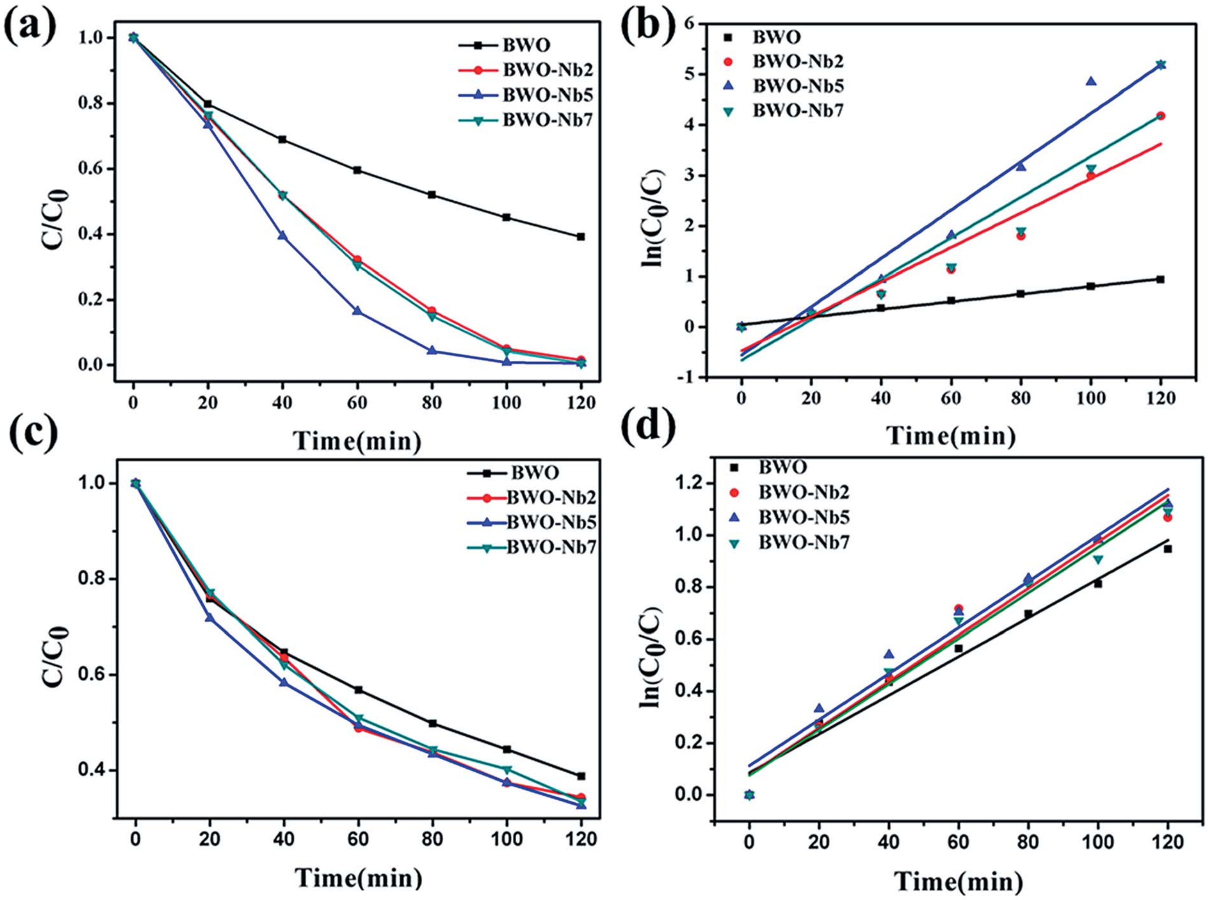

Fig. 10 (a) Dynamic curve of RhB over different samples; (b) photodegradation rates of RhB over different samples; (c) dynamic curve of TC over BWO-Nb and BWO; (d) photodegradation rates of TC over BWO-Nb and BWO.

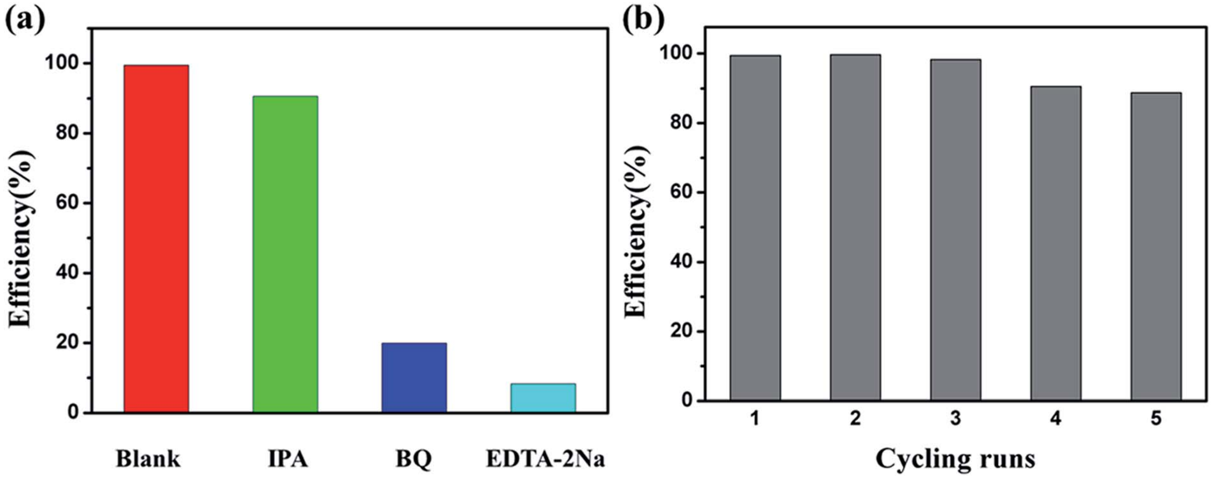

Fig. 11 (a) Photocatalytic degradation of RhB over BWO-Nb5 photocatalysts alone and with the addition of IPA, BQ, or EDTA-2Na; (b) photocatalytic degradation of RhB cycling test of BWO-Nb5.

irradiation time (t). The photocatalytic activities of all Nb-doped Bi_2WO_6 are better than pure Bi_2WO_6. In more detail, the degradation rate of BWO-Nb5 was 6.373 times that of BWO in the degradation of rhodamine B; the degradation rate of BWO-Nb5 was 1.4 times that of BWO in the degradation of TC.

In order to reveal the photocatalytic mechanism of BWO-Nb5 photocatalyst, we selected the main active substance capture agent for photocatalytic degradation experiments in Fig. 11a. With the addition of isopropanol (IPA, 2 mM, hydroxyl radical scavenger), the degradation efficiency of RhB was not significantly reduced, indicating that hydroxyl ($\cdot OH$) is not the main active substance for RhB degradation. However, when the scavenger benzoquinone (BQ, 0.1 mM) was added to scavenge the superoxide radical $\cdot O_2^-$, the degradation profile of RhB was significantly reduced. The results show that superoxide radical $\cdot O_2^-$ is one of the active substances degraded by RhB. When disodium edetate (EDTA-2Na, 10 mM) was used to remove photogenerated holes (h^+) in the reaction system, BWO-Nb5 hardly degraded RhB. The results of photocatalytic mechanism experiments show that $\cdot OH$ has little effect on the photodegradation process of RhB, h^+ and $\cdot O_2^-$ are the main active substances.

As shown in Fig. 11b, in order to test the stability of BWO-Nb5, five cycles of photodegradation of the RhB experiment were tested, and the BWO-Nb5 catalyst did not show any significant loss of activity. Cycling experiments showed good photocatalytic degradation stability of BWO-Nb5.

4. Conclusions

In summary, Nb-doped Bi_2WO_6 nanosheets were successfully synthesized by a hydrothermal method. The oxygen vacancies in Bi_2WO_6 crystals can be regulated by adjusting Nb doping. It is obvious that the effect of Nb doping has two aspects: on the one hand, Nb doping produces oxygen vacancies, which reduces the optical band gap of Bi_2WO_6 and enhances the separation and transfer of photogenerated carriers; on the other hand, Nb doping reduced the crystal size of Bi_2WO_6 with a larger surface area. Hence, the Nb-doped Bi_2WO_6 exhibits enhance photocatalytic activities in degradation of RhB and TC under visible light irradiation compared with pure Bi_2WO_6.

Conflicts of interest

The authors confirm that they have no conflict of interest.

Acknowledgements

This work is supported by The National Key Research and Development Program of China (No. 2016YFB0701100) and Key Research and Development Program of Zhejiang Province (No. 2017C01002).

References

1 A. Fujishima and K. Honda, *Nature*, 1972, **238**, 37.
2 M. A. Fox and M. T. Dulay, *Chem. Rev.*, 1993, **93**, 341–357.
3 O. Legrini, E. Oliveros and A. Braun, *Chem. Rev.*, 1993, **93**, 671–698.
4 Y.-S. Chang, M. Choi, M. Baek, P.-Y. Hsieh, K. Yong and Y.-J. Hsu, *Appl. Catal., B*, 2018, **225**, 379–385.
5 Y. H. Chiu, T. H. Lai, C. Y. Chen, P. Y. Hsieh, K. Ozasa, M. Niinomi, K. Okada, T. M. Chang, N. Matsushita, M. Sone and Y. J. Hsu, *ACS Appl. Mater. Interfaces*, 2018, **10**, 22997–23008.
6 R. Asahi, T. Morikawa, H. Irie and T. Ohwaki, *Chem. Rev.*, 2014, **114**, 9824–9852.
7 X. Yang, C. Cao, K. Hohn, L. Erickson, R. Maghirang, D. Hamal and K. Klabunde, *J. Catal.*, 2007, **252**, 296–302.
8 X. Zhang, X. Li, D. Zhang, N. Q. Su, W. Yang, H. O. Everitt and J. Liu, *Nat. Commun.*, 2017, **8**, 14542.
9 Y. Zhou, Z. Tian, Z. Zhao, Q. Liu, J. Kou, X. Chen, J. Gao, S. Yan and Z. Zou, *ACS Appl. Mater. Interfaces*, 2011, **3**, 3594–3601.

10 A. Kania, E. Talik, M. Szubka, W. Ryba-Romanowski, A. Niewiadomski, S. Miga and M. Pawlik, *J. Alloys Compd.*, 2016, **654**, 467–474.

11 L. Ye, J. Liu, C. Gong, L. Tian, T. Peng and L. Zan, *ACS Catal.*, 2012, **2**, 1677–1683.

12 P. Ju, Y. Wang, Y. Sun and D. Zhang, *Dalton Trans.*, 2016, **45**, 4588–4602.

13 M. Yoshino, M. Kakihana, W. S. Cho, H. Kato and A. Kudo, *Chem. Mater.*, 2002, **14**, 3369–3376.

14 N. Lv, Y. Li, Z. Huang, T. Li, S. Ye, D. D. Dionysiou and X. Song, *Appl. Catal., B*, 2019, **246**, 303–311.

15 P. Dumrongrojthanath, A. Phuruangrat, S. Thongtem and T. Thongtem, *Mater. Lett.*, 2017, **209**, 501–504.

16 R. Shi, G. Huang, J. Lin and Y. Zhu, *J. Phys. Chem. C*, 2009, **113**, 19633–19638.

17 M. Shang, W. Wang, L. Zhang and H. Xu, *Mater. Chem. Phys.*, 2010, **120**, 155–159.

18 X. C. Song, W. T. Li, W. Z. Huang, H. Zhou, H. Y. Yin and Y. F. Zheng, *J. Nanopart. Res.*, 2015, **17**, 134.

19 R. Cao, H. Huang, N. Tian, Y. Zhang, Y. Guo and T. Zhang, *Mater. Charact.*, 2015, **101**, 166–172.

20 N. Tian, Y. Zhang, H. Huang, Y. He and Y. Guo, *J. Phys. Chem. C*, 2014, **118**, 15640–15648.

21 H. Huang, K. Liu, K. Chen, Y. Zhang, Y. Zhang and S. Wang, *J. Phys. Chem. C*, 2014, **118**, 14379–14387.

22 H. Li, W. Li, F. Wang, X. Liu and C. Ren, *Appl. Catal., B*, 2017, **217**, 378–387.

23 H. Li, H. Hao, S. Jin, W. Guo, X. Hu, H. Hou, G. Zhang, S. Yan, W. Gao and G. Liu, *Catal. Commun.*, 2017, **97**, 60–64.

24 L. Zhang, Y. Man and Y. Zhu, *ACS Catal.*, 2011, **1**, 841–848.

25 J. Di, C. Zhu, M. Ji, M. Duan, R. Long, C. Yan, K. Gu, J. Xiong, Y. She, J. Xia, H. Li and Z. Liu, *Angew. Chem., Int. Ed. Engl.*, 2018, **57**, 14847–14851.

26 J. Di, C. Chen, C. Zhu, M. Ji, J. Xia, C. Yan, W. Hao, S. Li, H. Li and Z. Liu, *Appl. Catal., B*, 2018, **238**, 119–125.

27 C. Zhang and Y. Zhu, *Chem. Mater.*, 2005, **17**, 3537–3545.

28 Y. Chen, W. Yang, S. Gao, C. Sun and Q. Li, *ACS Appl. Nano Mater.*, 2018, **1**, 3565–3578.

29 J. Li, Z. Liang, L. Guo, N. Lei and Q. Song, *Mater. Lett.*, 2018, **223**, 93–96.

30 H. Fu, L. Zhang, W. Yao and Y. Zhu, *Appl. Catal., B*, 2006, **66**, 100–110.

31 C. Li, G. Chen, J. Sun, J. Rao, Z. Han, Y. Hu, W. Xing and C. Zhang, *Appl. Catal., B*, 2016, **188**, 39–47.

32 D. Wang, Y. Zhen, G. Xue, F. Fu, X. Liu and D. Li, *J. Mater. Chem. C*, 2013, **1**, 4153–4162.

33 W. C. Huo, X. a. Dong, J. Y. Li, M. Liu, X. Y. Liu, Y. X. Zhang and F. Dong, *Chem. Eng. J.*, 2019, **361**, 129–138.

34 Y.-H. Chiu, K.-D. Chang and Y.-J. Hsu, *J. Mater. Chem. A*, 2018, **6**, 4286–4296.

35 Y. H. Lu, W. H. Lin, C. Y. Yang, Y. H. Chiu, Y. C. Pu, M. H. Lee, Y. C. Tseng and Y. J. Hsu, *Nanoscale*, 2014, **6**, 8796–8803.